Electrode Materials for Enhancing the Performance and Cycling Stability of Zinc Iodide Flow Battery at High Current Densities

Fatemeh ShakeriHosseinabad, [†] Brandon Frost, [‡] Samia Said, [‡] Chaochen Xu, [¶] Diba Behnoudfar, [§] Kiana Amini, [//] Damilola Momodu, [†] Nader Mahinpey, [†] Philip Egberts, [¶] Thomas S. Miller, [‡] and Edward P.L. Roberts [*, †]

[†] *Department of Chemical and Petroleum Engineering, University of Calgary, 2500 University Drive NW, Calgary, Alberta, Canada T2N 1N4*

[‡] *Electrochemical Innovation Lab, Department of Chemical Engineering, University College London, London WC1E 7JE, United Kingdom*

[¶] *Department Mechanical and Manufacturing Engineering, University of Calgary, 2500 University Drive NW, Calgary, AB T2N 1N4, Canada*

[§] *School of Mechanical, Industrial, and Manufacturing Engineering, Oregon State University, Corvallis, OR 97331, USA*

[//] *Harvard John A. Paulson School of Engineering and Applied Sciences, 29 Oxford Street, Cambridge, MA, 02138 USA*

[⊥] **Corresponding author: Edward.P.L Roberts*

E-mail: Edward.Roberts@ucalgary.ca

Abstract

Aqueous redox flow battery systems that use a zinc negative electrode have a relatively high energy density. However, high current densities can lead to zinc dendrite

growth and electrode polarization, which limit the battery's high power density and cyclability. In this study, a perforated copper foil with a high electrical conductivity was used on the negative side, combined with an electrocatalyst on the positive electrode in the zinc iodide flow battery. A significant improvement in the energy efficiency (ca. 10% vs. using graphite felt on both sides) and cycling stability at a high current density of 40 mA cm^{-2} was observed. The long cycling stability with a high areal capacity of 222 mAh cm^{-2} is obtained in this study which is the highest reported areal capacity for zinc-iodide aqueous flow batteries operating at high current density, in comparison to previous studies. Additionally, the use of a perforated copper foil anode in combination with a novel flow mode was discovered to achieve consistent cycling at exceedingly high current densities greater than 100 mA cm^{-2}. In-situ and ex-situ characterization techniques, including in-situ atomic force microscopy coupled with in-situ optical microscopy and x-ray diffraction, are applied to clarify the relationship between zinc deposition morphology on the perforated copper foil and battery performance in two different flow field conditions. With a portion of the flow going through the perforations, a significantly more uniform and compact zinc deposition was observed compared to the case where all of the flow passed over the surface of the electrode. Results from modeling and simulation supports the conclusion that the flow of a fraction of electrolyte through the electrode enhances mass transport, and enabling a more compact deposit.

Key words: Zinc-iodide battery, Electrode materials, Zinc deposition, High current density, Battery performance, Cycling stability, In-situ electrochemical atomic force microscopy

Introduction

Aqueous zinc-based flow batteries have the benefits of high theoretical energy density, being constructed from environmental friendly, abundant, and low cost active materials, and inherent safety.[1,2] However, the potential for achieving high power density and long cycle

life is hindered by dendrite formation.[3] In zinc-based batteries, the properties of zinc metal allow for a high theoretical storage capacity, and low electrochemical potential.[4,5] The use of iodide for the positive electrolyte has the advantage of fast kinetics, high reversibility,[2,6,7] and high solubility in water (over 8 mole L^{-1}), enabling high theoretical energy density.[2,8] The highest reported catholyte-based discharge energy density for all aqueous flow batteries is 304 Wh L^{-1}, for the zinc iodide flow battery (ZIFB) at a current density of 10 mA cm^{-2}.[8] In addition, the appropriate I_3^-/I^- redox potential (0.536 V vs SHE) enables the prevention of water splitting.[8,9] Furthermore, zinc iodide flow batteries demonstrate high energy density by employing an electrolyte system with ambipolar characteristics.[2] This attribute indicates that the same electrolyte volume system can be used on both sides. Additionally, the electrolyte system serves as a bifunctional system, where one of the active species functions as the charge carrier.[2]

The behavior of zinc deposition on the negative electrode has an influence on the battery performance, particularly areal capacity, coulombic efficiency, and cycling stability. [10,11] Due to high power and capacity limitations in zinc-based batteries, improvement in the zinc anode performance are needed to enhance these characteristics.[12,13] It is reported that at high current densities (>20 mA cm^{-2}), the rapidly decreased ion concentration at the interface aggravates the detrimental selective zinc deposition and increases the rate of dendrite growth, leading to a decrease in rechargeability and cyclability.[4,14,15]

The Zn negative electrode has shown significant challenges in plating/stripping reactions.[16,17] To prevent dendrite formation at high current densities, a highly conductive electrode material on the negative side can be used that also achieves a more uniform interfacial electric field, as well as increaseed rechargeability and cycling stability of the battery.[4,18] Electrons and ions play a key role in the quality of zinc deposition,[4] thus optimizing the composition and interactions of the zinc electrode/electrolyte interface materials is important for designing dendrite-free anodes.[4] When using the non-conductive materials as coating layers, the performance is limited by electron/iontransportation.[19] These non-conductive materials

can promote side reactions on the Zn electrode, leading to accumulation of zinc deposition upon cycling and hence loss of rechargeability and battery failure.[19,20] Thus, the structural and conductive network of the zinc anode is important to limit the zinc dendrite growth.[4] The uniform interfacial electric field during zinc deposition, decrease in local current density, and specific areal capacity are necessary to optimize and stabilize the zinc deposition.[4,19]

Different types of the electrode such as zinc plate, carbon based material, copper foil, and copper foam have been used as the anode in zinc based batteries.[13,15,18,21–23] Zinc plate is not an appropriate host for zinc deposition because it causes random zinc growth and cracks.[21] Due to the lower binding energy between the zinc atom and carbon compared to that between the zinc atom and zinc surface, Zn^{2+} faces challenges in adsorbing onto a carbon surface and shows a greater affinity for being plated on the initially nucleated zinc deposits rather than on the remaining carbon surface.[4,15] The conductive carbon-based protective layer causes a uniform current distribution over the electrode surface and dendrite suppression, long cycle life, and enhanced areal capacity.[13] An epitaxial mechanism of deposition is reported for a graphene-based anode in metal-based batteries with high reversibility.[23,24] Tin sulfide (SnS) layer was used on the surface of the Zn metal anode in an aqueous zinc metal battery, serving as a regulating layer for Zn^{2+} ions and anions.[25] This stable SnS layer enhances the hydrophilicity at the interface, mitigates corrosion, and restricts the lateral movement of Zn^{2+} ions on the electrode surface. In order to create efficient aqueous zinc- based batteries and supercapacitors, a Bi-based energizer was added directly on the surface of the Zn anode.[26] This energizer not only improved the corrosion resistance of the zinc anode but also created a large number of nucleation sites for the deposition and dissolution of Zn. The creation of durable quasi-solid zinc metal batteries was reported by Guo et al.[27] They formed stable dual interphases between the electrolyte and electrode, which enhance the battery's electrochemical stability throughout its cycling process.

It was found that copper has intrinsic zincophilicity, making it suitable as an electrode material in zinc batteries.[21] The unique in-situ Cu-Zn solid solution layer on the copper

surface enhances the formation of a uniform zinc deposition during the electrochemical reaction.[21] Recently, the copper foil was used as an effective material to minimize lithium dendrite growth in an anode-free lithium metal battery.[28] The high electrical conductivity of copper foil creates a steady, uniform interfacial electric field during zinc deposition.[4] Using a copper foil anode with a flat surface leads to a uniform perpendicular distribution of electric field, and thus prevention of the charge accumulation on the anode surface.[4] The crystal plane of commercial copper foil can be modified to promote the dendrite-free zinc deposition.[29,30] Also, due to the inherent excellent electrical conductivity and open structure of porous 3D copper, the copper foam was used for zinc-ion batteries, and stable cycling performance during the plating/stripping processes was observed.[18]

To develop ZnIFBs with high capacity and long cycle life, a high-performance cathode material should be applied to match the stable Zn anode.[18] In the previous studies, cathode material such as metal-organic framework (MOF)-modified graphite felt, which involved Lewis acid sites as the catalytic sites,[31] and encapsulated iodine in the microporous carbon[32] were used in the positive electrode of ZnIFB contributing solid-liquid conversion reactions, but chemical, mechanical and electrochemical stability of these materials needs to be improved.[33] Currently, carbon-based materials are the best known for positive side electrodes in the zinc-based flow batteries.[1,34] A recent study, using a non-flow setup, has demonstrated a zinc-iodine aqueous battery that can operate without an ion exchange membrane, by utilizing a functionalized graphene electrode to immobilize the triiodide.[35] Nitrogen's electronegativity is believed to induce positively charged kinetic sites that likely enhance polyiodide anchoring and kinetics in N-doped reduced graphene oxide electrodes.[35] Anchoring polyiodides within the N-doped cathode with the enhanced adsorption capability can inhibit polyiodide shuttling, which leads to long-term stability in zinc-iodine batteries.

Conducting polymer polyaniline (PANI) is a typical conductive polymer[36,37] used as a polyiodide binder at the cathode to prevent the loss of charge products.[37–40] Poor kinetic reversibility of I_3^-/I^- on the graphite felt in the ZnIFB resulted in low energy efficiency.[31,37,40]

Pyrolized PANI has used as the electrode material for the ZnIFB owing to its rapid redox kinetics for improving the stability of ZnI batteries.[37,39–41] A pyrolized iron-PANI composite has also been demonstrated to deliver enhanced electrochemical performance in supercapacitors.[36]

The use of electrolyte additives[9,42] such as NH_4Br[43] and acetonitrile[44] in the zinc iodide electrolyte, has enhanced the cyclability and areal capacity of the zinc-iodide battery. This is due to the prevention of dendrite formation and enhancing the kinetic of I^-/I^-_3

Polyethylene glycol was added to create an aqueous/organic hybrid electrolyte for the zinc metal batteries with V_2O_5 nH_2O cathode. This approach effectively restricts the reac- tivity of free water molecules and diminishes the occurrence of adverse side reactions, such as cathode dissolution, zinc dendrites, and H_2 evolution.[45] In an aqueous zinc ion battery, a $ZnSO_4$ solution with $NaClO_4$ as the electrolyte prevented side reactions. Simultaneous insertion/extraction of Zn^{2+} and H^+ occurred in the NaKVOH cathode, significantly boosting specific capacity. The added ClO_4^- resulted in the formation of $Zn_4ClO_4(OH)_7$ on the cathode and formed a protective layer of Cl^- on the anode surface. This stable interface suppressed Zn dendrite growth and the hydrogen evolution reaction, enabling stable cycling.[46]

In our previous study,[3] a combination of a more uniform electric field and improved mass transport to achieve higher zinc ion concentration at the electrode/electrolyte interface will minimize the possibility of dendrite formation.[20,47] In this study, an additive-free system is considered to focus on two factors (potential distribution and zinc ion concentration).

To assemble a high-performance zinc-iodide battery at a current density of 40 mA cm^{-2} and 55% state of charge (SOC), we applied a perforated copper foil coupled with carbonized PANI (C-PANI) coated graphite felt. This assembly of electrodes has shown reduced polarization, stable cycling performance, and stable high values charge efficiencies. Due to inherent excellent electrical conductivity, a uniform deposition of Zn metal on the perfo- rated copper foil firmly seated over the current collector was observed. With C-PANI-coated graphite felt on the positive side of the battery, increased performance was observed, which

could be due to improved kinetic reversibility of I_3^-/I^- and chemical stability of C-PANI in the ZnI electrolyte solution.[37]

The mechanisms of electrochemical nucleation and growth of metal deposition in a battery device are very complex. Determining the role of the different factors influencing performance is challenging because the interfacial electrochemistry is coupled with potential distribution in the electrode and electrolyte, and the ion transport processes.[48] In a recent study for the zinc-bromine battery, in-situ electrochemical atomic force microscopy (EC- AFM) was conducted; it was shown that the formation of dense blocky Zn is controlled by instantaneous nucleation in the concentrated electrolytes. In dilute electrolytes, Zn becomes mossy as a result of progressive nucleation. [49] In-situ optical microscopy was conducted in previous studies,[50,51] and it was reported that the reaction kinetics and dendrite formation are affected by geometry and ion concentration of the anode. In our previous study,[3] we applied optical profilometry and X-ray computed tomography for evaluation of the zinc deposition in two different arrangements, but these methods can not efficiently provide the structure of deposited zinc. We present a comprehensive experimental study (i.e., in-situ and ex-situ analyses) to investigate the morphology of zinc deposition and the performance of the battery in two different flow modes. To understand the growth process and morphology of Zn deposition on the perforated copper foil, ex-situ and in-situ EC-AFM analyses coupled with ex-situ and in-situ optical microscopy were conducted in this study. We present an X-ray powder diffraction (XRD) analysis to investigate the dominant plane and uniformity of deposited zinc on the perforated copper foil. Scanning electron microscopy (SEM) and energy dispersive X-ray microscopy (EDX) analyses are applied to observe the morphology of zinc deposition and the structure of C-PANI on the graphite felt.

Experimental Details and Methods

Flow battery test cell

Details of the zinc-polyiodide flow cell design for performance analysis are provided in our previous study.[3] A photograph of the assembly using a perforated copper foil and graphite plate used in the battery is shown in Figure S1. In the test cell, a copper foil and C-PANI-coated graphite felt were used as the electrode on the negative and positive sides of the battery, respectively, except where indicated. The copper foil (purity: 99%, thickness: 0.004 inches, McMaster-Carr) was polished with grinding paper (P600) and washed with deionized water. Polishing the zinc anode before electrochemical operation will change the initial roughness of the Zn electrode surface and provide more nucleation sites and inhibiting dendrite formation.[51,52] This process can also influence the plating/stripping morphology during the cycling process.[51]

Nafion 117 was used as the separator, and 3M ZnI was used as the electrolyte. The electrode area of the battery was 5 cm^{-2}. Electrochemical measurements were conducted with a Biologic potentiostat with an electrochemical impedance spectroscopy (EIS) module. Charge-discharge experiments were performed at constant current densities in the range of 10-40 mA cm^{-2}. EIS was conducted for a frequency range from 200 kHz to 0.1 Hz. The negative electrode was thoroughly rinsed to remove any ZnI_2 electrolyte prior to ex-situ imaging and characterization.

Characterization of Zinc deposition

In-situ AFM and Optical Microscopy: The detailed design of the half-cell for in-situ optical microscopy and AFM analysis is shown in Figure 1 and Figure S2. In the horizontal half-cell design, a perforated copper block with a surface area of 1.7 cm^{-2} was used as the negative electrode (see Figure 1 (a)). The three operating modes, flow-by (FB), flow-through (FT), and flow-by-through (FBT), were obtained using the valves on the outlet of the cell. In

the FB mode, the valve located at the top exit of the cell was opened while the valve at the bottom exit of the test cell was closed. In the FT operating mode, the valve located at the top exit of the cell was closed while the valve at the bottom exit was opened. This created a flow of electrolyte through the electrode perforations, so the electrolyte was forced to flow through the electrode perforations. In the FBT design, all valves in the FBT design were opened, dividing the flow of electrolyte between both pathways. The perforated Cu piece was polished (circular for 5 min) with grinding papers (BUEHLER silicon carbide) of P2500 and P600 and washed with deionized water before being used as the working electrode (See Figure 1 (b) and Figure S2 (a)). Zn foils (purity: 99%, thickness: 0.5 mm, Sigma-Aldrich) were washed with deionized water before using as the counter and reference electrodes (see Figure S2 (b)). The electrolyte contained 3 M ZnI_2 (ZnI_2, 98% Thermo Fisher Scientific) in deionized water (PURELAB Option-Q, 18.2 MΩ). Both in-situ optical microscopy and EC-AFM experiments were conducted using a Gamry electrochemical workstation (Interface 1000 Potentiostat) to apply a constant current (10 mA cm^{-2}) to the working electrode. In- situ optical microscopy (Keyence Digital Microscope VHX-7000) images were obtained for all FB, FT, and FBT configurations after pausing the process at 5 seconds, 15 seconds, and 50 seconds of electrodeposition. 3D images were obtained by a depth composition process, which is achieved by automatically scanning the optical lens throughout the different focal planes. The surface roughness values, the arithmetical mean deviation of the surface height from the mean height (S_a) and root mean squared (S_q), were obtained by AFM for the whole area of the captured images. In-situ EC–AFM (Bruker Dimension Icon with ScanAsyst) experiments were carried out using ScanAsyst tapping mode with a Scout 150 silicon probe with a reflective Al coating (Nu Nano., k = 18 N m^{-1}, f_0 = 150 kHz). Images were captured for FB, FT, and FBT configurations while the electrochemical process was paused at 5 seconds, 15 seconds, and 50 seconds of plating. All of the results obtained from the AFM were analyzed by Gwyddion software.

Ex-situ AFM and Optical Microscopy: A MFP3D AFM (Asylum Research) was em-

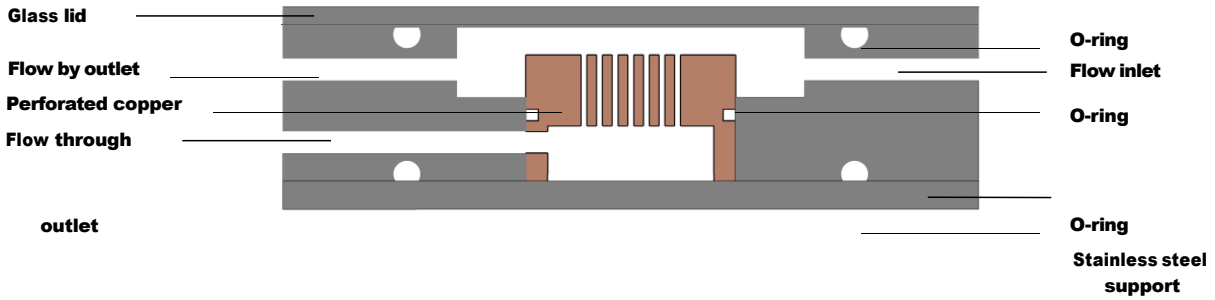

(a)

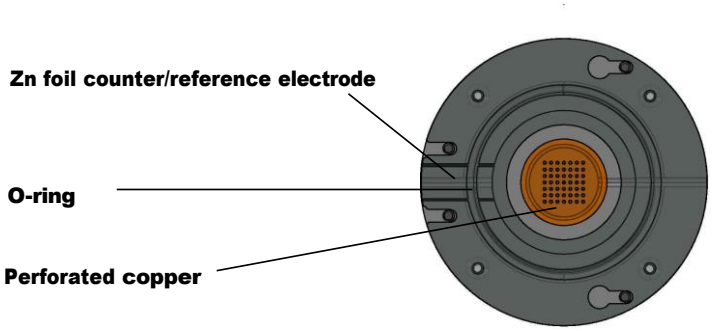

(b)

Figure 1: Schematic illustration of the in-situ AFM test cell, showing (a) a cross section through, and (b) a plan view of the cell. Different electrolyte flow modes were applied using valves in the outlet ports, including FB, where electrolytes flowed across the surface of the perforated working electrode, flow-through, where all of the electrolytes flowed through the electrode on each side of the cell; and FBT mode where some of the electrolytes flowed through the perforated electrode and remainder flowed across the surface. Electrolyte flowing through the electrode exited via a manifold under the current feeder below copper foil.

ployed to perform the AFM measurements in ambient conditions (20-25˚C, relative humidity 20%). Topography and phase images were obtained using tapping mode with a silicon tip (Nanaosensors PPP-NCL). The mapping area was 3 µm × 3 µm, and the scanning velocity was 3 µm s^{-1}. For ex-situ optical microscopy, the perforated copper foil was placed directly under the 20 × objective of a Leica microscope, followed by image processing to determine roughness parameters.

SEM: A quanta FEG 250 FESEM (Thermo Fisher Scientific) was used to obtain SEM images of the electrode. The SEM was equipped with a Bruker Esprit X-ray microanalysis system consisting of a Quantax 5030 energy-dispersive X-ray (EDX) spectrometer, Bruker SVE signal processing unit, and Esprit version 2.2 software. All imaging and analyses were performed under high-vacuum conditions with an accelerating potential ranging from 5 kV to 15 kV. EDX analysis was performed at different locations to evaluate the uniformity of distribution. The SEM-EDX map of carbon and nitrogen of the positive electrode (C-PANI coated on graphite felt) is shown in Figure S3 (a-c). EDX spectrum of C-PANI coated on felt is shown in Figure S4. N atoms can increase the electrode's hydrophilicity and the wettability of the electrode.[53]

The presence of defects facilitates the diffusion and adsorption of the reactant species. [54]

XRD and Raman analysis: To evaluate the effect of flow field design on initial zinc deposition on perforated copper foil, the ex-situ X-ray diffraction (XRD) analysis was used to identify the crystallinity of the sample. XRD was carried out via a Rigaku ULTIMA III X-ray diffractometer. XRD was performed on zinc deposited on copper foil electrode after a short-run charging in the flow battery test cell. The samples were scanned (ex-situ) over two theta ranges of 10-90 ˚ at the rate of 0.003 deg min^{-1}. The XRD results were analyzed with Bruker XRD search and match program EVA. The Raman spectra of C-PANI coated on graphite felt were obtained using a WITec alpha 300 R Confocal Raman microscope (WITec GmbH, Germany). C-PANI coated on graphite felt characterized by XRD and Raman, indicated that the D-to-G band ratio decreases in electrodes coated with C-PANI compared

to heated graphite felt, possibly due to the strain induced by PANI on the felt's structural framework (shown in Figure S5). Further discussion of Raman and XRD characterization of the C-PANI coated on graphite felt has been included in section 1 of the supplementary information.

Catalyst preparation: To synthesize PANI, 0.2 M aniline hydrochloride was added to a 50 ml solution of 1.0 M HCl, and in a separate beaker, 0.25 M solution of ammonium persulphate was added to 1.0 M HCl. The prepared solutions were kept at room temperature for one hour; thereafter, they were mixed and stirred for about an hour and left to polymerize.

After polymerization, PANI precipitate was collected on a filter (after being washed several times with 100 ml of 0.2 M HCl and acetone) and dried at 60 ˚C overnight. Thereafter, the slurry was brushed uniformly on the graphite felt, with a loading of 8 mg cm^{-2}, which was placed in a tube furnace and heated to 850 ˚C and pyrolyzed for 2 h under an N_2 atmosphere, to obtain a C-PANI modified graphite felt.[36] The nitrogen functional groups in PANI, can provide more active adsorption sites for the I_3^-/I^- leading to facile reaction kinetics of I_3^-/I^-.[37,55] The three different electrode materials used in the ZnIFB experiments, i.e., perforated copper foil, graphite felt, and carbonized PANI modified graphite felt, are denoted: Cu, GF, and C-PANI-GF, respectively.

Modeling and assumptions: The simulation of zinc plating and distribution was conducted in a 2.2 cm × 2.2 cm in a half-cell electrodeposition system (shown in Figure S6). A constant zinc ion source was added uniformly in order to simulate the reaction current. The study employs several standard equations including conservation of species, velocity and pressure fields, Nernst-Planck equation, Faraday's law, Butler-Volmer equation, and electroneutrality equation.[56,57] To simulate the FBT flow mode, the perforations were simulated as additional outlets through the electrode. A constant velocity was used as the inlet boundary condition, while constant pressure was assumed at all outlets. The SI provides comprehensive information about the equations and boundary conditions.

The model is subject to the following simplifying assumptions:

- Electrochemical kinetics were assumed to be described by the Butler-Volmer equation.
- Electrochemical rate constants were assumed to be approximately constant, i.e. the effects of temperature, electrode-fouling, etc. were not included.
- The effect of adsorption, capacitance, electrodes/endplates resistivity, and shunt currents were assumed to be negligible.
- The current efficiency was assumed to be 100% and side reactions were not considered.
- The flow of electrolyte is assumed to be laminar, and the electrolyte itself is assumed to be an incompressible fluid.
- Dilute solution theory is employed for the electrolyte.
- The battery functions within an isothermal condition.
- In the FBT mode, the flow of electrolyte through the perforated electrode was approximated using an outlet region, corresponding to perforation, with a co-located continuous surface for the electrode and the outflow boundary.

Results and discussion

Performance analysis

Performance analysis and charge/discharging voltage profiles of ZnIFB using FB and FBT flow modes with graphite felt baseline electrodes are shown in our previous study.[3] This study investigated the ZnIFB performance using a perforated copper foil negative electrode and C-PANI modified graphite felt positive electrode using FB and FBT operating modes. The impact of the C-PANI modification of the positive electrode on the charge/discharge behavior of the ZnIFB (with a perforated copper negative electrode and FBT flow mode) is shown in Figure 2 (a) and (b). The modification of the positive electrode with the nitrogen

functional groups obtained from pyrolyzed PANI led to a reduction in the overpotentials (and thus increased voltage efficiency) at current densities from 20-40 mA cm^{-2}. This is consistent with previous studies that have shown the benefit of C-PANI carbon for I_3^-/I^- redox system due to increased surface area and electrochemical activity of modified electrode.[37]

The cycling stability and performance of the ZnIFB was evaluated at a current density of 40 mA cm^{-2} using a C-PANI-coated graphite felt on the positive and graphite felt negative electrode. Limited cyclability was observed in this case, with the battery efficiency dropping off rapidly after around 40 cycles (shown in Figure 2 (c)). In contrast, with a copper foil negative electrode, stable cycling was observed with both FBT and FB operating modes for 100 cycles (see Figures 2 (d) and S7). These results confirm that the low stability in the cycling of the ZnIFB is most likely due to the irreversible zinc plating/stripping process with a graphite felt negative electrode.

For comparison cyclability and performance of ZnIFB with a copper foil on the negative side and graphite felt on the positive side were investigated and shown in Figure S8. Around 5% improvement in the performance compared with the baseline electrodes at a higher current density of 40 mA cm^{-2} was observed. Performance analysis confirms that applying C-PANI, on the negative side, has not enhanced the reversibility of zinc plating/stripping (See Table 1 and Figure S9).

The cyclability and performance of the battery at a current density of 40 mA cm^{-2} was evaluated with the pair of electrodes of C-PANI-coated graphite felt on the positive and perforated copper foil on the negative side. In two different flow field designs, FB and FBT, a charge efficiency of ca. 96% and ca. 99% was observed during cycling, respectively. The battery was tested over 100 cycles, and stability in cycling was observed. The voltage efficiency and charge efficiency of the battery increased ca. 10% compared with the use of a graphite felt in both negative and positive electrodes operating in FBT mode. Cycling efficiency for FBT and FB modes are shown in Figures 2 (d) and S7. In the FBT mode, lower potential loss (and hence higher voltage efficiency and energy efficiency) were observed.

In both flow modes, the potential losses observed during charge-discharge cycles increased with current density as expected shown in Figure 2 (a) and (b), and our previous study.[3] The summary of performance and cyclability of the battery at a high current density of 40 mA cm^{-2} operating in FBT mode are shown in Table 1. Areal capacity is an important parameter to evaluate the volumetric capacity and cycling stability in solid-hybrid RFBs.[11] In this study, the ZNIFB at high current density has shown a higher areal capacity of 222 mAh cm^{-2} with the energy-to-power ratio of 5.6 hours[11] and high stability in cycling compared with the previous studies on ZnIFB (see Figure 2 (e) and Table S1).[2,5,8,9,11,43,44]

The combination of a perforated copper foil anode and the FBT flow mode was not only found to enable amongst the highest areal capacity ever achieved, it was also found to provide stable cycling at very high current densities of >100 mA cm^{-2}. Stability was achieved in the cycling of the ZnIFB with FBT mode at >140 mA cm^{-2} using a perforated copper foil on the negative side and graphite felt on the positive side. 150 cycles at a current density of 140 mA cm^{-2} and 1M ZnI_2, with an areal capacity of 46.7 mAh cm^{-2} is shown in Figure 2 (f). Also, stable coloumbic and energy efficiencies of ca. 84.5% and ca. 47%, respectively, were obtained. In contrast, with graphite felt electrodes operating in FBT mode, poor performance was observed at 140 mA cm^{-2}, and the battery could only be cycled for 10 cycles (shown in Figure S10). The poor cycling performance of graphite felt electrodes at high current densities (e.g., 140 mA cm^{-2}) in the ZnIFB can be attributed to several factors. At high current densities, the ion concentration at the interface rapidly decreases on the graphite felt, which increases the cell voltage, side reactions, and dendrite growth.[3] This can lead to a decrease in rechargeability and cyclability. In addition, it has been shown that at high current density a solid film of iodine can form on the positive electrode leading to passivation.[44] The graphite felt cathode is not a suitable match for the graphite felt anode when used at high current densities in ZnIFB, which can result in limited cycling and a significant decrease in capacity.

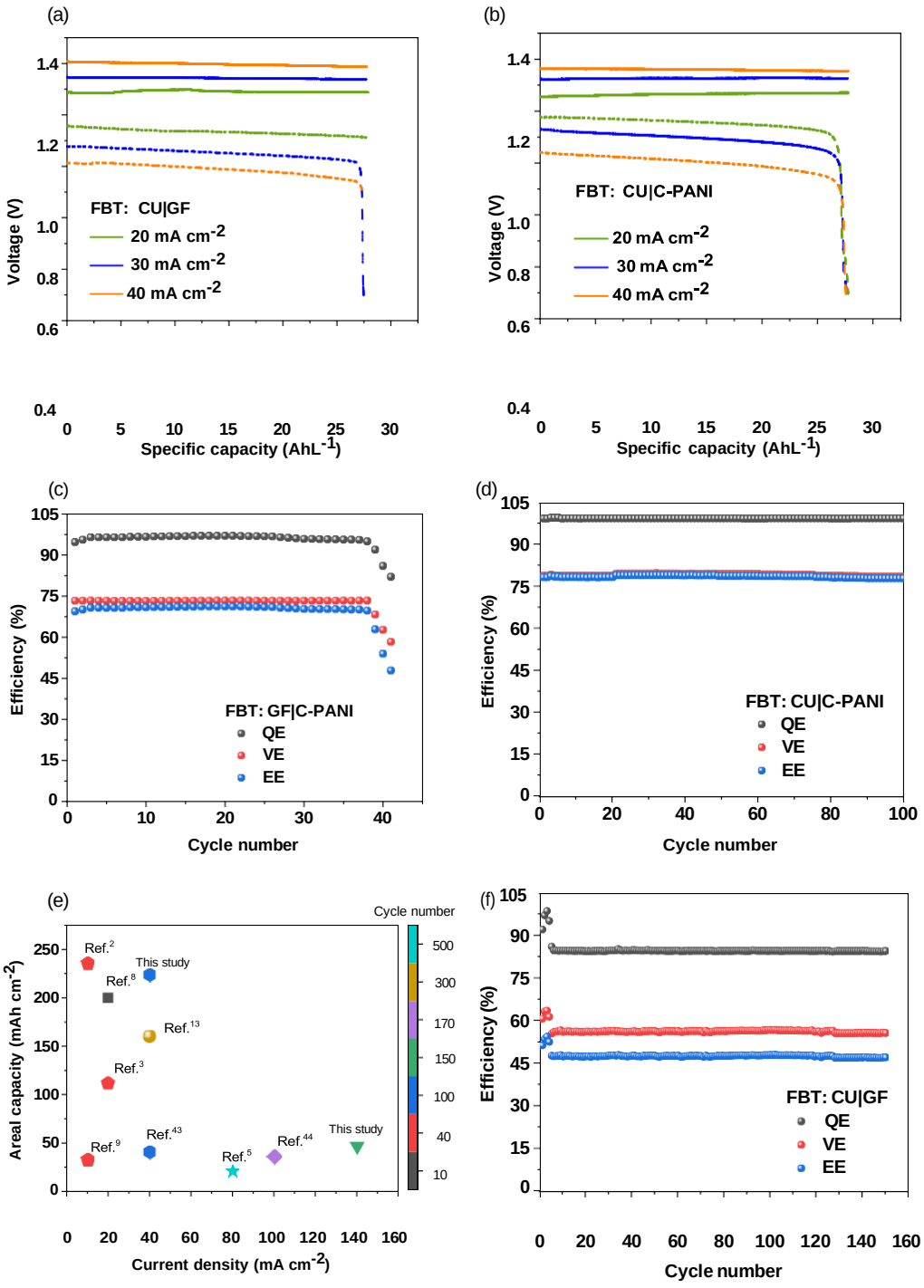

Figure 2: Galvanostatic charge-discharge voltage profile for a ZnIFB using a 3 M ZnI_2 electrolyte (20 mL on each side) at constant current densities of 20, 30, and 40 mA cm^{-2}, charging to 27.5% SOC (areal capacity of 111 mAh cm^{-2}), operating in FBT mode with two pairs of electrodes. **(a)** CU(negative)|GF (positive), **(b)** CU (negative)|PANI (positive). Efficiencies during charge-discharge cycling of a 5 cm^2 ZnIFB using a 3 M ZnI_2 electrolyte (20 mL on each side) using a constant current density of 40 mA cm^{-2} charged to 55% SOC on each cycle (areal capacity 222 mAh cm^{-2}), and operating in FBT mode, **(c)** GF (negative)|C- PANI (positive), and **(d)** CU(negative)|C-PANI(positive). **(e)** Zinc-iodide batteries analyzed based on areal capacity,

current density, and cycle number (color map). **(f)** Efficiencies during charge-discharge cycling of a ZnIFB using a 1 M ZnI_2 electrolyte (20 mL on each side) using a constant current density of 140 mA cm^{-2} and 150 cycles (areal capacity of 46.7 mAh cm^{-2}), and operating in FBT mode. QE, VE, and EE stands for coloumbic efficiency, voltage efficiency and energy efficiency, respectively.

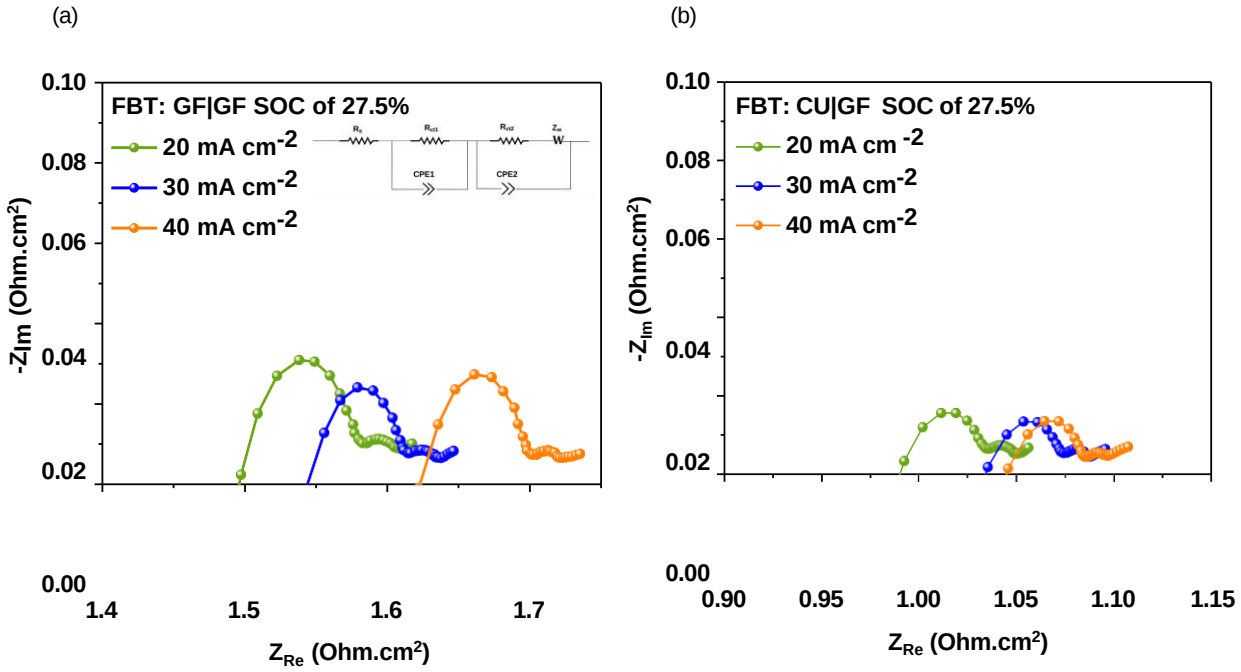

Figure 3: In-situ EIS analysis of a 5 cm^2 flow battery using a 3 M ZnI_2 (20 mL on each side), at 27.5% SOC with Nafion 117 under constant current densities in a range of 20, 30, and 40 mA cm^{-2} at FBT mode with the schematic of an equivalent circuit for the EIS of the ZnIFB **(a)** GF|GF, and **(b)** CU(negative)|GF(positive).

EIS analysis

In-situ EIS was carried out using different pairs of electrodes such as graphite felt on the positive and negative sides, graphite felt on the positive side and perforated copper foil on the negative side (see Figure 3), and carbonized-PANI-coated graphite felt on the positive and perforated copper foil on the negative side (see Figure S11) in the ZnIFB setup. The measurements were conducted at a range of current densities from 20 to 40 mA cm^{-2} and a SOC of 27.5% while operating in FBT mode.

The high-frequency intercept of the EIS curve with the real impedance axis indicates the ohmic resistance of the cell. Equivalent circuit parameter values are selected based on models proposed in previous studies of Zinc iodide batteries.[20,37,58] The ohmic and charge transfer resistance were evaluated by fitting the EIS data using the equivalent circuit shown in Figure 3. R_S represents the ionic resistance of the solution and the internal resistance of electrodes. Rct_1 and Rct_2 are attributed to the charge transfer resistance at the electrode-electrolyte

interfaces for the anode and cathode.[37,58] The values of these parameters obtained are shown in Table S2.

The charge transfer resistance was observed to decrease with increasing current density in a range of 20 to 40 mA cm^{-2} (see Figure 3), consistent with the previous studies.[20,59,60] In contrast, the ohmic resistance increased with the current density, possibly due to build up/precipitation of I_2 on the positive electrode[44,61] or due to the presence of a tough zinc deposition and prevention of ion diffusion and electron conduction.[14,62] By applying copper foil on the negative side and FBT mode of operation, the ohmic and charge transfer resistances decreased by around 50% compared to a ZnIFB using graphite felt (see Figure 3 (a) and (b)) and Table S2. In spite of its much lower surface area, zinc deposition is promoted on the copper foil leading to reduced charge transfer resistance, consistent with previous studies on other zinc-based batteries.[20,60] It has been shown that the $CuZn_5$ forms on the surface of the copper foil, facilitating uniform zinc deposition.[21]

Table 1: Zinc-Iodide Battery Charge/Discharge Performance at a Current density of 40 mA cm^{-2} as a Function of Electrode Material in FBT Mode.

Combination of electrodes (positive and negative)	Charge efficiency (%)	Voltage efficiency (%)	Energy efficiency (%)	Number of cycles
GF|GF	96.5	69.4	67	<40
C-PANI(-)|GF	97	70	67.9	<40
C-PANI|C-PANI	97	72	69.9	<40
GF(-)|C-PANI	97	73.2	71	<40
CU(-)|GF	99	72.7	72	100
CU(-)|C-PANI	99.2	76.07	76	100

Analytical and Spectroscopy Analysis

SEM characterization:

The morphology of zinc deposition on the perforated copper foil was evaluated for the FB and FBT flow modes after the 100th charging cycle with the pair of electrodes of C-PANI-caoted graphite felt on the positive and perforated copper foil on the negative side in the ZnIFB at 55% SOC (corresponding to an areal capacity of 222 mAh cm^{-2}) at a current density of

40 mA cm^{-2} (Figure 4). In both cases, a relatively uniform zinc deposition was observed (see Figure 4 (b) and (c)). The uniform zinc deposition is likely due to the low nucleation overpotential, and homogeneous electric field distribution on the copper electrode.[18,63] Zinc nucleation overpotentials have previously been reported to be 9.5 mV and 45.3 mV for copper and carbon electrodes, respectively.[21]

It was shown that Cu foam or foil exhibits complete exfoliation of zinc arrays, enabling a remarkable zinc reversible stripping/plating.[63]

With the FB mode, Figure 4 (b), although the deposit is uniform, a lateral and somewhat porous deposition can be observed, indicating higher overpotential during zinc deposition. The higher overpotential leads to an increased growth rate of zinc islands,[64] and the formation of larger sized crystals and a more porous structure.

In the FBT design, a layer-like and compact deposition with a smaller size of zinc flakes was observed (see Figure 4 (c)). The improvement in the deposit morphology in the FBT mode is likely due to improved ion/mass transport through the perforated copper, associated with the addition of flow towards the current feeder (through the perforation).

A high-resolution SEM-image of C-PANI-coated graphite felt compared with the pristine felt is shown in Figure 4 ((d) and (e)), a micro-nano structure of PANI with irregular porous structure distributed on the felt fibers is observed.

XRD analysis of zinc deposition:

Ex-situ XRD patterns of zinc deposition on the perforated copper foil after 300 and 1000 seconds of charging were collected for two different flow modes, FB and FBT (see Figure 5). It was reported that zinc deposition with (002) plane, indicating basal plane oriented crystals, provides a thermodynamically stable orientation.[49,65] Zn growth with the plane of (102) and (101) was reported for the alignment of 30–70˚ of the deposited crystal.[66,67] The dominant planes in the XRD pattern after 1000 s deposition are (102), (103), (100), (002), (110), (112), (004), and (201), which are consistent with the literature.[14,67,68] Previous

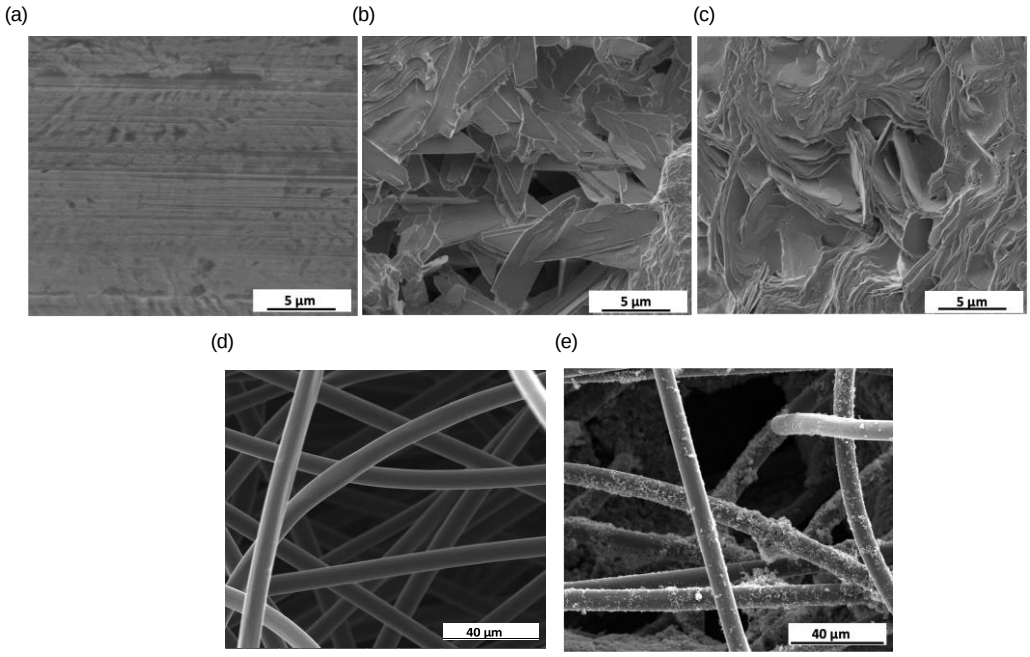

Figure 4: SEM images of (a) pristine copper foil, and the surface of the zinc electrode in the ZnIFB after the 100th cycle at SOC of 55% (areal capacity of 222 mA cm^{-2}) with a 3 M ZnI_2 electrolyte at a current density of 40 mA cm^{-2}, operated in (b) FB and (c) FBT mode. SEM images of (d) pristine graphite felt, and (e) C-PANI graphite felt.

studies have reported a layer like deposit of zinc with growth on the microstep edges.[69] Free energy analysis has shown that zinc deposits with basal plane (002) orientation are thermodynamically favored.[49] Pyramid structures of basal plane 002 orientation is favorable for achieving uniform zinc deposition.[24] In the current study, the XRD and ex-situ AFM analysis confirmed the basal deposition with the (002) plane for operation in FBT flow mode. A zinc deposit with a pyramid hexagonal shape approximately parallel to the copper substrate was observed, which is beneficial for a uniform deposit and cyclability.[24] In FB flow mode, the basal facet with (002) plane orientation was also observed in the XRD results. However, as zinc deposition continued in the FB design, additional facets with a rougher, more porous morphology were observed in SEM and ex-situ AFM images.

Zn deposition with the strong (110) surface planes, deposited crystal has the alignment of 70–90° [66,67] and zinc deposition is likely to produce dendrite formation.[18,66] The plane of (110) is observed in the zinc deposition after 1000 seconds in the FB mode, shown in Figure 5

(c). In the XRD of the zinc deposition, the plane of (004) (Figure 5 (d)) observed in the FBT mode with higher intensity indicates better zinc deposition and a more regular crystalline arrangement of the deposited zinc on copper.[70] Based on the XRD patterns obtained from zinc deposition after 1000 s of charging, the intensity (counts) of the diffraction peaks in the FBT mode was higher than in FB mode. Also, the peak related to the (103) plane in the zinc deposition in the FBT mode is more uniform (See Figure 5 (c) and (d)).

AFM analysis

AFM analysis is applied as a valuable technique to investigate morphological and mechanical properties of the deposited zinc on the copper electrode when the ZnIFB is under electro-chemical control.[71] AFM analyses (in-situ and ex-situ), coupled with optical microscopy (in-situ and ex-situ), were applied to analyze the morphology, roughness, and growth rate of the deposited zinc under different flow modes (FB, FT, and FBT).

Ex-situ AFM analysis:

A comparison of the ex-situ AFM analysis of zinc deposition after charging for 600 seconds at 20 mA cm^{-2} in FB and FBT modes are shown in Figure 6 (Morphology (a) and (d), 3D morphology ((b) and (e)), and phase map (c) and (f)). In the FB mode, the morphology of zinc crystal deposition is non-uniform and rough, indicating more defects on the surface (see Figure 6 (a-c)). In contrast, in the FBT design, due to a better mass/ion transfer a hexagonal smoother shape with a pyramid appearance and sharp edges is observed (see Figure 6 (d-f)). A hexagonal and smoother shape deposit was reported under improved mass transport conditions, where the surface concentration of zinc is uniform and close to the bulk concentration.[3,49]

The average roughness values obtained from morphology data (height images) for FB and FBT are 96.42 nm and 11.69 nm respectively. It is well known that the phase signal obtained by the AFM tapping mode represents changes in the energy dissipation of the

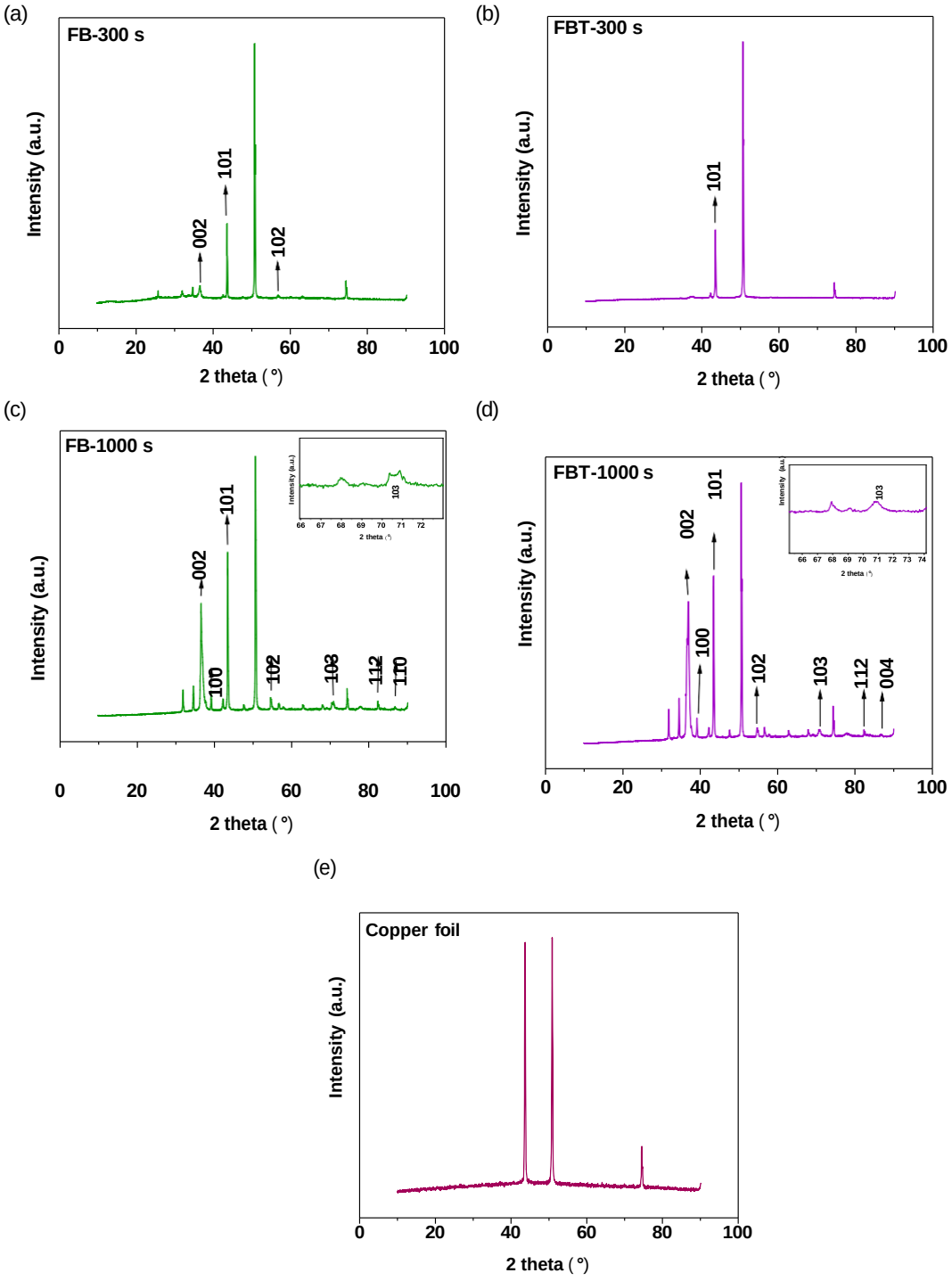

Figure 5: Ex-situ XRD patterns of (a) zinc deposition on copper foil after 300 s of charging for FB, (b) zinc deposition on copper foil after 300 s charging for FBT, (c) zinc deposition on copper foil after 1000 s charging for FB, (d) zinc deposition on copper foil after 1000 s charging for FBT, and (e) copper foil substrate of a 5 cm^2 flow battery using a 3 M ZnI_2 electrolyte (20 mL on each side) under a constant current density of 20 mA cm^{-2} with Nafion 117.

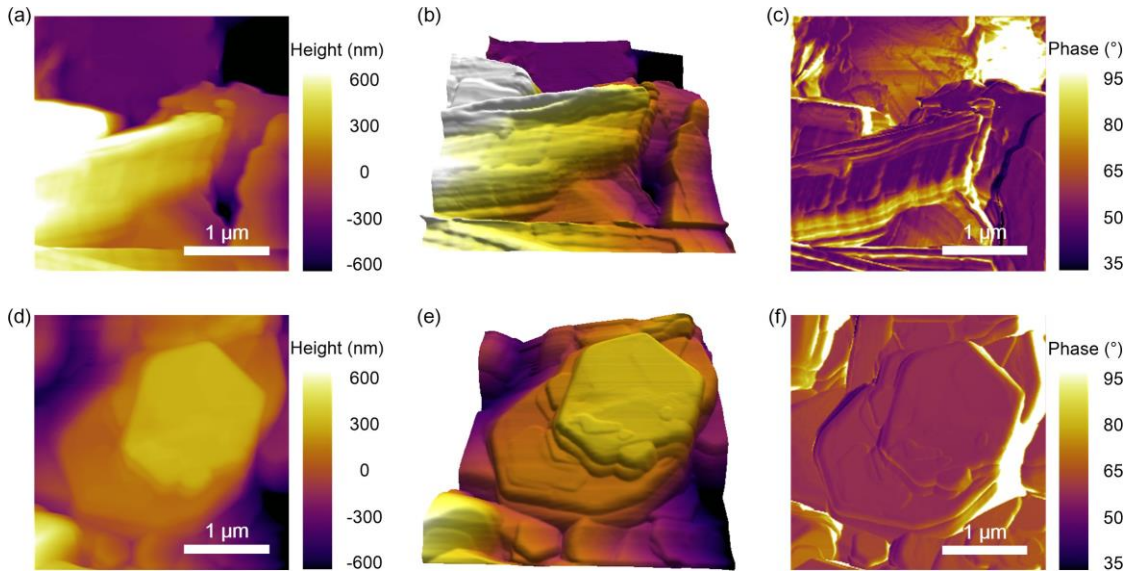

Figure 6: Ex-situ AFM images for two different flow field designs after 600 s charging under a current density of 20 mA cm^{-2} (areal capacity of 0.17 mA cm^{-2}). Morphology **(a)**, 3D morphology **(b)** and phase map **(c)** of zinc deposition on a copper foil substrate in a conventional FB design. Morphology **(d)**, 3D morphology **(e)** and phase map **(f)** of another zinc deposition on a copper foil substrate operated in the FBT mode from the surface between the perforations.

oscillating cantilever as it scans over the surface,[72,73] that can be used provide a map of effective stiffness,[74,75] i.e., the zinc deposition. Typically, a material with lower stiffness tends to exhibit a smaller phase value.[76,77] Figure 6 (c) and (f) show the phase signal over the zinc deposited on a perforated copper foil using FB and FBT modes. The FBT mode shows a higher stiffness as indicated by its higher average phase angle of 58.23 ˚, compared to the FB mode with an average phase angle of 51.07 ˚. Furthermore, the lower standard deviation of the phase value (0.32 ˚) in FBT mode compared to that in FB mode (3.08 ˚) suggests a more uniform distribution of zinc deposition in the FBT mode compared to the FB mode. Ex-situ optical microscopy analysis was performed of the zinc deposit prepared in under the same conditions as those shown in Figure 6 and similar findings were obtained (see Figure S12) with a smoother, more uniform deposit.

Note that AFM and optical microscopy images were obtained at the initial stages of the deposition (600 s at 20 mA cm^{-2}, 0.17 mAh cm^{-2}) and cannot be directly compared with SEM images shown in Figure 4, which were after 100 cycles and a much longer deposition

(20000 s at 40 mA cm^{-2}, 222 mAh cm^{-2}). However, a comparison of initial structure from the AFM images and final morphology seen in the SEM images confirms the presence of a more uniform deposition in the FBT mode.

In-situ AFM analysis:

In-situ AFM images coupled with in-situ optical microscopy obtained under constant current 10 mA cm^{-2} are shown in Figure 7, Figure S13, and Figure S14 for each flow mode: a) FB; b) FT; and c) FBT. Figures 7 a-c (i) show the pristine copper electrode, under electrolyte at open circuit voltage (OCV). For each flow mode (a-c), the initial stages of zinc nucleation and deposition onto the perforated Cu electrode were visualized at 5s (ii), 15s (iii) and 50s (iv) of charging. Height profiles were measured by line scan analysis across the dotted black lines in the AFM images shown in Figure S13, and are presented in Figure S15. The mean roughness and root mean squared roughness (S_a and S_q), and their percentage increase as a function of time from the pristine values were all calculated from the height profiles in Figure S15, and are presented in Table 2. Additionally, from Figure 7, it can be clearly seen that the flow mode significantly influences the rate of nucleation and final morphology of the deposits. In the FB system, it can be seen that after 5s of charging, (Figure 7 a (ii)) a number of zinc particles of varying sizes (between 121 nm – 1.61 µm) nucleate across the surface of the Cu electrode with a random distribution, when compared to the pristine electrode (Figure 7 a (i)). This results in a S_a and S_q increase of 100% and 127%, respectively. After 15s of charging (Figure 7 a (iii), particles begin to agglomerate, forming an inhomogeneous surface layer with larger zinc deposits (147 nm – 2.42 µm). The surface S_a and S_q has increased further to 333% and 357%, respectively. Finally, after 50 s of charging, the particles have completely agglomerated, to form two large zinc dendrites, with a multi-micron variation in height (Figure 7 a (iv)), and the S_a and S_q have both increased by nearly ×40. In the FT system (Figure 7 b) it appears the rate of nucleation is greater than in the FB system, as after 5s of applied current (Figure 7 b (ii)), although the nucleation sites appear to be similar,

deposits are larger in size and more compact, resulting in a greater increase in S_a and S_q of 218% and 238 %, compared to the pristine Cu electrode (Figure 7 b (i)). After 15s of applied current (Figure 7 b (iii)), the size of the Zn deposits have become more varied (ranging from 208 nm – 2.88 µm) and appears more boulder-like; however, the surface of the Cu electrode is no longer visible which suggests the deposits are more densely packed on its surface, and therefore a decrease in surface roughness between 5 and 15 s of charging (S_a and S_q of 122% and 131%). Finally, after 50 s of applied current (Figure 7 b (iv)) the boulder-like shape of the deposits had become more pronounced as well as the variation in height, and the final roughness has now increased to ca. 360% for both S_a and S_q. Lastly, in the FBT system as shown in Figure 7 c, it appears the rate of nucleation has significantly decreased, such that after 5 seconds of applied current (Figure 7 c (ii)), when compared to the other flow modes in Figure 7 a (ii) and Figure 7 b (ii), nucleation sites are smaller and of similar sizes (86-718 nm), and dispersed evenly and compactly across the Cu electrode surface. This resulted in a modest increase in the electrode S_a and S_q of 79% and 76%. After 15 seconds (Figure 7 c (iii)), there is a uniform increase in the size of the Zn deposits, and the Cu electrode surface is still visible which is testament to the greater packing density imposed by the FBT mode. This is reflected further by the low increase in surface roughness S_a and S_q of 108% and 106%, respectively. Even after 50 s of applied current (Figure 7 c (iv)) the electrode surface features were still visible. Additionally, the shapes of the deposits were distinct from those in Figure 7 a and b (iv) in that they were not boulder-like in shape, rather more faceted, and the surface was flatter with less height variation. The final surface roughness for each flow system after 50s of charging increased in the order of FB > FT > FBT, with S_a measured at 1.03 > 0.261 > 0.226 µm, and S_q measured at 1.2 > 0.344 > 0.301 µm respectively. It can therefore be concluded that, a more uniform and smooth deposition was observed in the FBT mode compared to both FB and FT arrangements. In the FB and FT modes, zinc clusters were evident earlier than in the FBT mode. The early deposition/nucleation of zinc in the FB and FT modes could be due to the presence of higher overpotential, resulting from

higher mass transfer resistance overcoming the energy barrier of the nucleation.[14]

The growth rate of the zinc was obtained based on the maximum peak height after 50 s and is summarized in Table S3. The error bars for the values obtained for roughness and growth rate are shown in Figure S16. The growth rate of the zinc deposition in the FBT mode is ca. 4.5 ± 1.4 nm s^{-1}, which is much slower than that of the FB (10.1 ± 6 nm s^{-1}) and FT (12.9 ± 1.4 nm s^{-1}) modes, consistent with a more compact and smoother deposit in FBT mode. The growth rate of zinc deposit and rate of nucleation increase with increasing the overpotential.[57]

3D in-situ optical microscopy images are shown in Figure S17, a thick and rough deposition is observed in the FB mode (shown in Figure S17 (a) compared with FT (shown in Figure Figure S17 (b)) and FBT (shown in Figure S17 (c)) designs. A thin, compact, and smooth zinc deposition is observed in the FBT mode. The roughness of zinc deposition in FT mode is more than the deposition in the FBT arrangement.

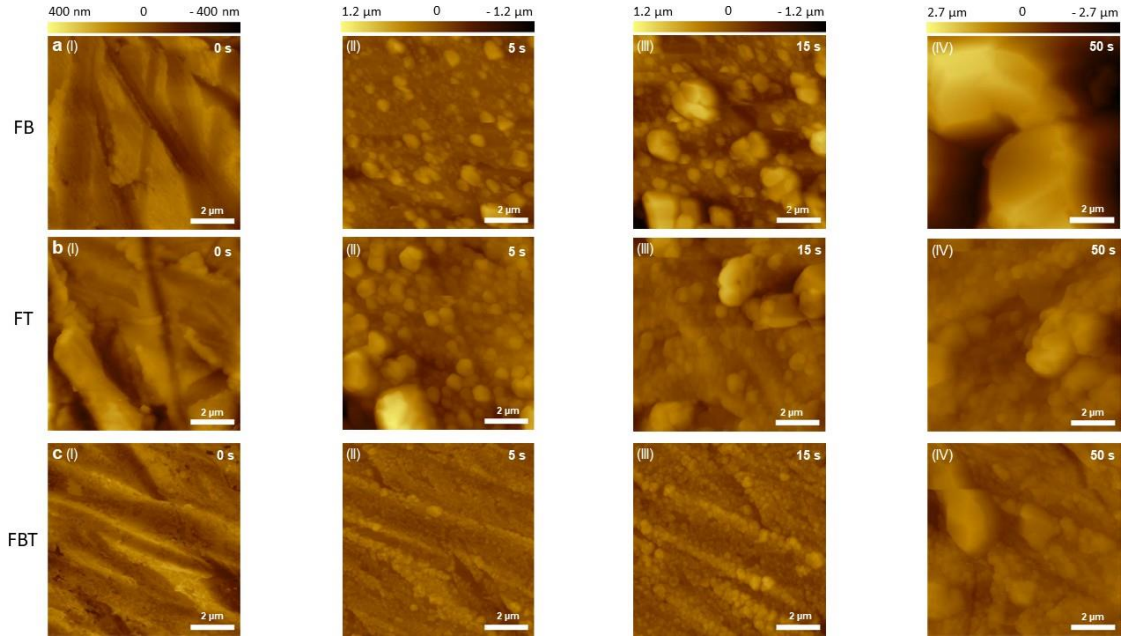

Figure 7: In-situ AFM images of Zn electrodeposits on perforated copper foil during the first 50 s of deposition in the half cell and show the surface between perforations, shown in Figure 1, using 3 M ZnI_2 at a current density of 10 mA cm^{-2}. **a (I-IV)** FB flow mode, **b (I-IV)** FT flow mode, **c (I-IV)** FBT flow mode. All images show the surface between the perforations.

Table 2: Roughness Analysis Obtained from in-Situ AFM Data Shown in Figure 7

Flow Mode	0 s	5 s	15 s	50 s	%increase (0-5 s)	%increase (0-15 s)	%increase (0-50 s)
FB	S_a: 50.9 nm	S_a: 101.7 nm	S_a: 220.3 nm	S_a: 1037.1 nm	S_a: 99.8	S_a: 332.8	S_a: 1937.3
	S_q: 61.4 nm	S_q: 140.0 nm	S_q: 281.1 nm	S_q: 1184.9 nm	S_q: 128.0	S_q: 357.6	S_q: 1829.3
FT	S_a: 56.2 nm	S_a: 178.42 nm	S_a: 124.58 nm	S_a: 260.50 nm	S_a: 217.6	S_a: 121.7	S_a: 363.7
	S_q: 74.3 nm	S_q: 251.16 nm	S_q: 171.86 nm	S_q: 344.4 nm	S_q: 237.8	S_q: 131.1	S_q: 363.2
FBT	S_a: 48.3 nm	S_a: 86.50 nm	S_a: 100.53 nm	S_a: 226.25 nm	S_a: 78.4	S_a: 107.8	S_a: 367.8
	S_q: 62.7 nm	S_q: 110.30 nm	S_q: 128.97 nm	S_q: 301.72 nm	S_q: 75.9	S_q: 105.7	S_q: 381.2

S_a: Mean roughness; S_q: Root mean squared of roughness

Modeling of zinc deposition on copper foil

Simulation of zinc deposition in batteries was carried out in several studies.[20,47,60] In this study a two-dimensional (2-D) model for zinc deposition on a non-porous perforated copper foil is developed with COMSOL Multiphysics in both FB and FBT modes, considering charge and mass conservation. The schematic diagram of the 2-D geometry of the negative half cell of ZnIFB is shown in Figure 8 (a). The x-direction is the distance from the electrode surface towards the membrane direction, and y-direction is oriented towards the surface of the electrode. The geometry and dimensions of the battery incorporated in the model are listed in Table S4.

On the perforated copper foil, the electrolyte flows across and through the non-porous electrode. The perforated electrode is placed at X = 0 and position 1, and the electrolyte flows along the electrode surface in the length of $0 \leq h \leq H$. The inlet and outlet are located at positions 2 and 3, and the membrane is located at position 4. The inlet flow rate for both flow modes is the same, but in the FBT mode, the amount of flow passing through the electrode (the flow through outlet region labaled in Figure 8 (a)) is two times higher than that passing across the electrode.

As mentioned in the AFM and optical microscopy analysis sections, a more compact and smoother zinc deposit was observed on the surface of the electrode in the FBT flow mode. This effect was previously associated with the smaller difference between the surface concentration of Zn^{2+} and the bulk concentration due to the improved ion transport.[20,47,60] To

verify this, we mathematically model the problem using the conservation of mass, species, charge and momentum as detailed in the SI section. Figure 8 presents the solution to the problem using the conditions in Table S4. Due to the flow of a fraction of the electrolyte through the electrode in the FBT mode and the convective transport of ions to the electrode, the bulk electrolyte replenishes the depleted Zn^{2+}, and a higher Zn^{2+} concentration is obtained at the electrode surface (Figure 8 (b)). The velocity profiles for both flow modes, leading to different convective transport behaviors, are shown in Figure S18. The calculated electrolyte potential at the electrode surface (shown in Figure 8 (c)) is lower in FBT mode compared to FB mode which has implications for the smoothness of the deposited layer and prevention of dendrite formation. According to Ma MC et al.[78] an increase in the ion concentration on the electrode surface correlates with a smaller electrolyte potential which in turn results in a smoother deposition and suppression of the dendrites.

The variation of Zn^{2+} concentration with distance from the electrode surface is shown in Figure 8 (d-e), at three different positions, initial, halfway, and approaching the end along the electrode surface in the direction of flow. A higher gradient of Zn^{2+} concentration and bulk is obtained at the electrode/electrolyte interface in the FB mode compared with FBT mode along the electrode surface. Very low gradient Zn^{2+} concentration with the bulk in the FBT mode associated with a lower electrolyte potential resulting in a compact and smooth deposition on the electrode surface.[20,47,60]

Conclusion

For practical zinc-based batteries with long cycle life, it is essential to improve the Zn^{2+} transfer kinetics at high current densities. The stripping/plating process of Zn in aqueous batteries presents a challenge to the stable performance of zinc-based batteries. In this study, a pair of perforated copper foil negative electrode with high electrical conductivity, to give uniform potential combined with a recently demonstrated flow mode (FBT) to give

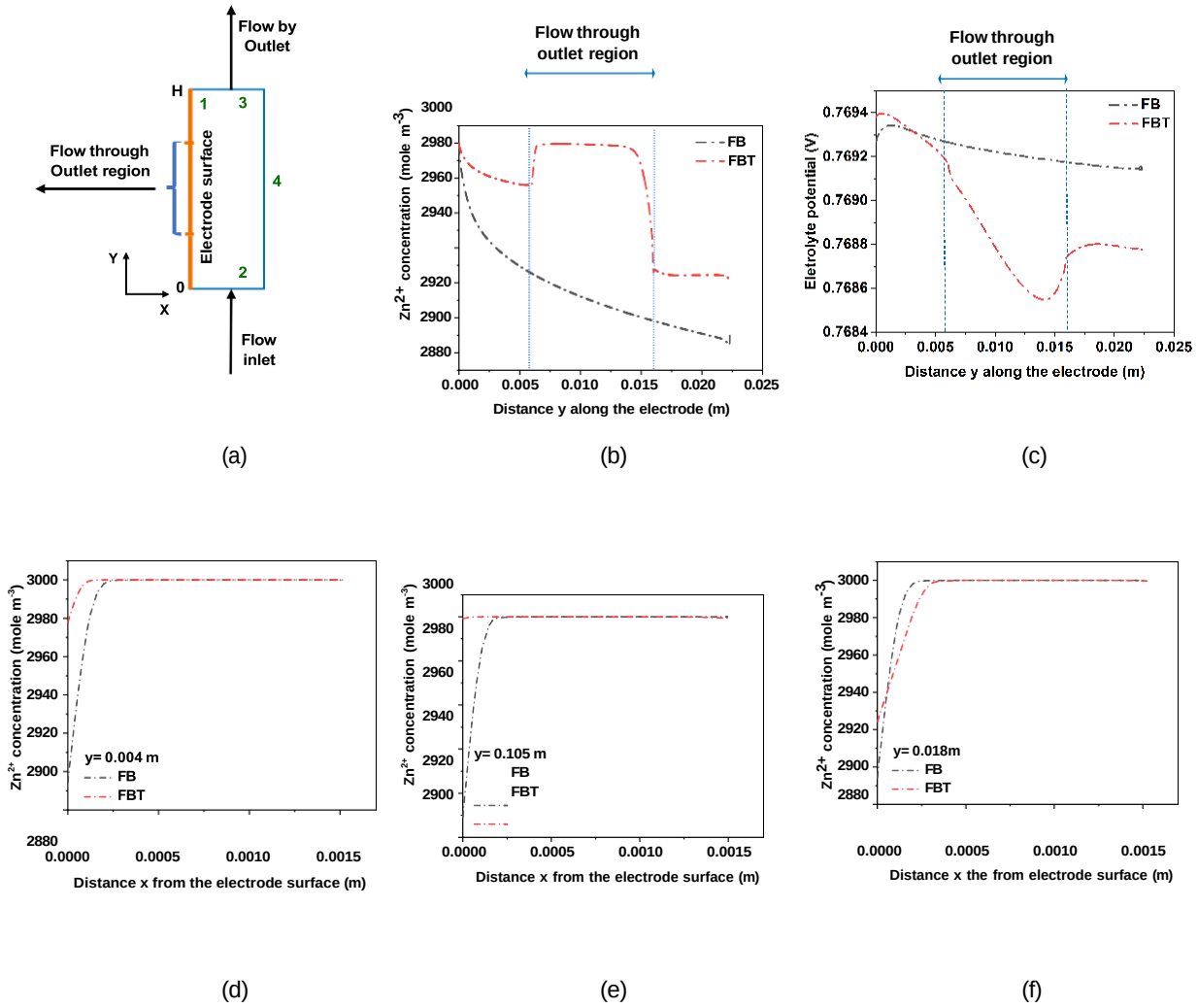

Figure 8: 2-D simulation of zinc deposition on perforated copper foil in FB and FBT modes. (a) Schematic diagram of 2-D model geometry of the negative half-cell of ZnIFB, (b) Zn^{2+} concentration along the electrode surface in FB and FBT modes, (c) the variation in the potential of the electrolyte for FB and FBT flow modes. The variation of Zn^{2+} concentration with distance from the electrode surface at three different positions along the electrode surface in the direction of flow in FB and FBT flow modes, (d) initial, (e) halfway, and (f) approaching the end.

a high mass transfer rate and thus uniform zinc ion concentration at the electrode, enabled a high-performance and cyclable ZnIFB at a high current density of 40 mA cm^{-2} and areal capacity of 222 mAh cm^{-2}. The areal capacity in this study is the highest areal capacity reported for the ZnIFB. Additionally, this combination demonstrated the ability to maintain stable cycling even under current densities exceeding 100 mA cm^{-2}.

Modified graphite felt positive electrode, using C-PANI, was used to ensure good performance at the positive side of the battery. The C-PANI modification gives lower overpotential due to the presence of more active sites, and faster reaction kinetics of the I_3^-/I^-.[37]

A combination of in-situ and ex-situ analyses was conducted to evaluate the effect of electrode materials and flow mode on the performance and cyclability of the battery. In-situ EIS analysis indicates that with a perforated copper foil negative electrode, the ohmic and charge transfer resistances were both around 50% lower than obtained with graphite felt. An investigation of the morphological evolution and electrochemical zinc deposition in different flow modes was conducted using in-situ and ex-situ EC-AFM analysis coupled with in-situ optical microscopy. The results showed that the FBT arrangement yielded a thinner and more uniform zinc deposit with lower roughness compared to the rough and thick deposition observed in the FB mode.

Theoretical modeling and simulation have verified that in the FBT mode, there is a higher concentration of Zn^{2+} on the electrode surface and a lower concentration gradient of Zn^{2+} between the surface and bulk. Additionally, it was obtained that the potential of the electrolyte in the FBT mode is lower than that in the FB mode. In the future, for practical applications of the novel design, modification of the surface of copper foil with multifunctional interface layers,[20] may enhance the areal capacity and stable cycling for large-scale grid storage applications.

Conflicts of interest

The authors declare no competing financial interest

Acknowledgements

This manuscript is the result of the research project funded by the Natural Science and Engineering Research Council of Canada (NSERC CREATE 495455-2017 and RGPIN-2018-03725) and STFC batteries network (ST/R006873/1). Financial support for this work is highly appreciated. S.S. acknowledges the EPSRC Centre for Doctoral Training in the Ad- vanced Characterisation of Materials (EP/S023259/1). T.S.M. and B.F. acknowledge sup- port from the Faraday Institution (EP/S003053/1) LiSTAR project (FIRG014, FIRG058).
C.X. acknowledges financial support from the University of Calgary Eyes High Postdoctoral Match Fellowship.

Author Contribution

Fatemeh ShakeriHosseinabad: Conceptualization of the study, methodology, experimental work and analysis, sample preparation, in-situ AFM cell design, preparation of the original manuscript draft. **Brandon Frost:** In-situ AFM analysis, editing, and reviewing the manuscript **Samai Said:** In-situ AFM analysis, editing, and reviewing of the manuscript, **Chaochan XU:** Ex-situ AFM analysis, editing, and reviewing of the manuscript, **Diba Behnoudfar:** COMSOL simulation and modeling conceptualization, **Kiana Amini:** COMSOL simulation and modeling conceptualization, **Damilola Momodu:** Electrocatalyst material, editing, and reviewing of the manuscript, **Nader Mahinpey:** Supervision and reviewing of the manuscript, **Philip Egberts:** Supervision of ex-situ AFM Characterization, editing and reviewing the manuscript, **Thomas Miller:** Supervision of in-situ AFM Characterization, editing, and reviewing the manuscript, **Edward P.L.Roberts:** Securing funding,

supervision, conceptualization of the study, editing, and reviewing of the manuscript.

Supporting Information Available

The following files are available free of charge.

- Battery test cell anode components
- In-situ AFM test cell images
- SEM Map and EDX spectrum of C-PANI on felt
- EIS analysis details
- Cycling at high current densities
- Details of AFM measurements
- 2D & 3D in-situ optical microscopy
- Details of modeling and simulation

References

(1) Yuan, Z.; Yin, Y.; Xie, C.; Zhang, H.; Yao, Y.; Li, X. Advanced materials for zinc-based flow battery: development and challenge. *Advanced Materials* **2019**, *31*, 1902025.

(2) Li, B.; Nie, Z.; Vijayakumar, M.; Li, G.; Liu, J.; Sprenkle, V.; Wang, W. Ambipolar zinc-polyiodide electrolyte for a high-energy density aqueous redox flow battery. *Nature communications* **2015**, *6*, 6303.

(3) ShakeriHosseinabad, F.; Daemi, S. R.; Momodu, D.; Brett, D. J.; Shearing, P. R.; Roberts, E. P. Influence of Flow Field Design on Zinc Deposition and Performance in a Zinc-Iodide Flow Battery. *ACS Applied Materials & Interfaces* **2021**, *13*, 41563–41572.

(4) Zhang, Q.; Luan, J.; Tang, Y.; Ji, X.; Wang, H. Interfacial design of dendrite-free zinc anodes for aqueous zinc-ion batteries. *Angewandte Chemie International Edition* **2020**, *59*, 13180–13191.

(5) Xie, C.; Liu, Y.; Lu, W.; Zhang, H.; Li, X. Highly stable zinc–iodine single flow batteries with super high energy density for stationary energy storage. *Energy & Environmental Science* **2019**, *12*, 1834–1839.

(6) Li, Z.; Weng, G.; Zou, Q.; Cong, G.; Lu, Y.-C. A high-energy and low-cost polysulfide/iodide redox flow battery. *Nano energy* **2016**, *30*, 283–292.

(7) Zhao, Y.; Wang, L.; Byon, H. R. High-performance rechargeable lithium-iodine batteries using triiodide/iodide redox couples in an aqueous cathode. *Nature communications* **2013**, *4*, 1–7.

(8) Zhang, J.; Jiang, G.; Xu, P.; Kashkooli, A. G.; Mousavi, M.; Yu, A.; Chen, Z. An all-aqueous redox flow battery with unprecedented energy density. *Energy & Environmental Science* **2018**, *11*, 2010–2015.

(9) Weng, G.-M.; Li, Z.; Cong, G.; Zhou, Y.; Lu, Y.-C. Unlocking the capacity of iodide for high-energy-density zinc/polyiodide and lithium/polyiodide redox flow batteries. *Energy & Environmental Science* **2017**, *10*, 735–741.

(10) Yang, Q.; Li, Q.; Liu, Z.; Wang, D.; Guo, Y.; Li, X.; Tang, Y.; Li, H.; Dong, B.; Zhi, C. Dendrites in Zn-based batteries. *Advanced Materials* **2020**, *32*, 2001854.

(11) Yao, Y.; Lei, J.; Shi, Y.; Ai, F.; Lu, Y.-C. Assessment methods and performance metrics for redox flow batteries. *Nature Energy* **2021**, *6*, 582–588.

(12) Lu, L.-L.; Ge, J.; Yang, J.-N.; Chen, S.-M.; Yao, H.-B.; Zhou, F.; Yu, S.-H. Free-standing copper nanowire network current collector for improving lithium anode performance. *Nano letters* **2016**, *16*, 4431–4437.

(13) Wang, S.; Yuan, C.; Chang, N.; Song, Y.; Zhang, H.; Yin, Y.; Li, X. Act in contravention: A non-planar coupled electrode design utilizing “tip effect” for ultra-high areal capacity, long cycle life zinc-based batteries. *Science Bulletin* **2021**, *66*, 889–896.

(14) Wang, K.; Pei, P.; Ma, Z.; Chen, H.; Xu, H.; Chen, D.; Wang, X. Dendrite growth in the recharging process of zinc–air batteries. *Journal of Materials Chemistry A* **2015**, *3*, 22648–22655.

(15) Yin, Y.; Wang, S.; Zhang, Q.; Song, Y.; Chang, N.; Pan, Y.; Zhang, H.; Li, X. Dendrite-free zinc deposition induced by tin-modified multifunctional 3D host for stable zinc-based flow battery. *Advanced Materials* **2020**, *32*, 1906803.

(16) Guo, N.; Huo, W.; Dong, X.; Sun, Z.; Lu, Y.; Wu, X.; Dai, L.; Wang, L.; Lin, H.; Liu, H., et al. A review on 3D zinc anodes for zinc ion batteries. *Small Methods* **2022**, *6*, 2200597.

(17) Wang, S.-B.; Ran, Q.; Yao, R.-Q.; Shi, H.; Wen, Z.; Zhao, M.; Lang, X.-Y.; Jiang, Q. Lamella-nanostructured eutectic zinc–aluminum alloys as reversible and dendrite-free anodes for aqueous rechargeable batteries. *Nature communications* **2020**, *11*, 1–9.

(18) Kang, Z.; Wu, C.; Dong, L.; Liu, W.; Mou, J.; Zhang, J.; Chang, Z.; Jiang, B.; Wang, G.; Kang, F., et al. 3D porous copper skeleton supported zinc anode toward high capacity and long cycle life zinc ion batteries. *ACS Sustainable Chemistry & Engineering* **2019**, *7*, 3364–3371.

(19) Zheng, X.; Ahmad, T.; Chen, W. Challenges and strategies on Zn electrodeposition for stable Zn-ion batteries. *Energy Storage Materials* **2021**, *39*, 365–394.

(20) He, M.; Shu, C.; Hu, A.; Zheng, R.; Li, M.; Ran, Z.; Long, J. Suppressing dendrite growth and side reactions on Zn metal anode via guiding interfacial anion/cation/H2O distribution by artificial multi-functional interface layer. *Energy Storage Materials* **2022**, *44*, 452–460.

(21) Zhang, Q.; Luan, J.; Fu, L.; Wu, S.; Tang, Y.; Ji, X.; Wang, H. The three-dimensional dendrite-free zinc anode on a copper mesh with a zinc-oriented polyacrylamide electrolyte additive. *Angewandte Chemie* **2019**, *131*, 15988–15994.

(22) Jiang, H.; Wu, M.; Ren, Y.; Shyy, W.; Zhao, T. Towards a uniform distribution of zinc in the negative electrode for zinc bromine flow batteries. *Applied energy* **2018**, *213*, 366–374.

(23) Zhang, K.; Yan, Z.; Chen, J. Electrodeposition accelerates metal-based batteries. *Joule* **2020**, *4*, 10–11.

(24) Zheng, J.; Zhao, Q.; Tang, T.; Yin, J.; Quilty, C. D.; Renderos, G. D.; Liu, X.; Deng, Y.; Wang, L.; Bock, D. C., et al. Reversible epitaxial electrodeposition of metals in battery anodes. *Science* **2019**, *366*, 645–648.

(25) Hu, Y.; Fu, C.; Chai, S.; He, Q.; Wang, Y.; Feng, M.; Zhang, Y.; Pan, A. Construction of zinc metal-Tin sulfide polarized interface for stable Zn metal batteries. *Advanced Powder Materials* **2023**, *2*, 100093.

(26) Wang, M.; Meng, Y.; Li, K.; Ahmad, T.; Chen, N.; Xu, Y.; Sun, J.; Chuai, M.; Zheng, X.; Yuan, Y., et al. Toward dendrite-free and anti-corrosion Zn anodes by reg- ulating a bismuth-based energizer. *eScience* **2022**, *2*, 509–517.

(27) Guo, S.; Qin, L.; Hu, C.; Li, L.; Luo, Z.; Fang, G.; Liang, S. Quasi-Solid Electrolyte Design and In Situ Construction of Dual Electrolyte/Electrode Interphases for High-Stability Zinc Metal Battery. *Advanced Energy Materials* **2022**, *12*, 2200730.

(28) Lai, G.; Jiao, J.; Fang, C.; Jiang, Y.; Sheng, L.; Xu, B.; Ouyang, C.; Zheng, J. The Mechanism of Li Deposition on the Cu Substrates in the Anode-Free Li Metal Batteries. *Small* **2022**, 2205416.

(29) Xie, Z.; Wu, Z.; An, X.; Yue, X.; Wang, J.; Abudula, A.; Guan, G. Anode-free rechargeable lithium metal batteries: progress and prospects. *Energy Storage Materials* **2020**, *32*, 386–401.

(30) Tang, B.; Fan, H.; Liu, Q.; Zhang, Q.; Liu, M.; Wang, E. Stable Sn@ Cu foam enables long cycling life of zinc metal anode for aqueous zinc batteries. *International Journal of Energy Research* **2022**, *46*, 18562–18572.

(31) Li, B.; Liu, J.; Nie, Z.; Wang, W.; Reed, D.; Liu, J.; McGrail, P.; Sprenkle, V. Metal–organic frameworks as highly active electrocatalysts for high-energy density, aqueous zinc-polyiodide redox flow batteries. *Nano letters* **2016**, *16*, 4335–4340.

(32) Pan, H.; Li, B.; Mei, D.; Nie, Z.; Shao, Y.; Li, G.; Li, X. S.; Han, K. S.; Mueller, K. T.; Sprenkle, V., et al. Controlling solid–liquid conversion reactions for a highly reversible aqueous zinc–iodine battery. *ACS Energy Letters* **2017**, *2*, 2674–2680.

(33) Fu, J.; Cano, Z. P.; Park, M. G.; Yu, A.; Fowler, M.; Chen, Z. Electrically rechargeable zinc–air batteries: progress, challenges, and perspectives. *Advanced materials* **2017**, *29*, 1604685.

(34) Munaiah, Y.; Suresh, S.; Dheenadayalan, S.; Pillai, V. K.; Ragupathy, P. Comparative Electrocatalytic performance of single-walled and multiwalled carbon nanotubes for zinc bromine redox flow batteries. *The Journal of Physical Chemistry C* **2014**, *118*, 14795–14804.

(35) Dang, H. X.; Sellathurai, A. J.; Barz, D. P. An ion exchange membrane-free, ultrastable zinc-iodine battery enabled by functionalized graphene electrodes. *Energy Storage Materials* **2023**, *55*, 680–690.

(36) Rantho, M.; Madito, M.; Manyala, N. Symmetric supercapacitor with supercapattery behavior based on carbonized iron cations adsorbed onto polyaniline. *Electrochimica Acta* **2018**, *262*, 82–96.

(37) Wu, W.; Li, C.; Wang, Z.; Shi, H.-Y.; Song, Y.; Liu, X.-X.; Sun, X. Electrode and electrolyte regulation to promote coulombic efficiency and cycling stability of aqueous zinc-iodine batteries. *Chemical Engineering Journal* **2022**, *428*, 131283.

(38) ShakeriHosseinabad, F.; Momodu, D.; Roberts, E. P. Electrode Materials for Enhancing the Performance of a Zinc Iodide Flow Battery at High Current Density. ECS Meeting Abstracts. 2021; p 113.

(39) Hilário, R. B.; de Moraes, T. H.; Gonçalves, J. M. d. R. P.; Gandara, M.; Gonçalves, E. S. Influence of heat treatment and electrochemical treatment on the properties of PANI electrodeposited on carbon fiber felt. *Diamond and Related Mate- rials* **2022**, *123*, 108867.

(40) Miao, X.; Chen, Q.; Liu, Y.; Zhang, X.; Chen, Y.; Lin, J.; Chen, S.; Zhang, Y. Performance comparison of electro-polymerized polypyrrole and polyaniline as cathodes for iodine redox reaction in zinc-iodine batteries. *Electrochimica Acta* **2022**, *415*, 140206.

(41) Shi, H.-Y.; Ye, Y.-J.; Liu, K.; Song, Y.; Sun, X. A Long-Cycle-Life Self-Doped Polyaniline Cathode for Rechargeable Aqueous Zinc Batteries. *Angewandte Chemie* **2018**, *130*, 16597–16601.

(42) Mitha, A.; Yazdi, A. Z.; Ahmed, M.; Chen, P. Surface Adsorption of Polyethylene Glycol to Suppress Dendrite Formation on Zinc Anodes in Rechargeable Aqueous Batteries. *ChemElectroChem* **2018**, *5*, 2409–2418.

(43) Jian, Q.; Wu, M.; Jiang, H.; Lin, Y.; Zhao, T. A trifunctional electrolyte for high-performance zinc-iodine flow batteries. *Journal of Power Sources* **2021**, *484*, 229238.

(44) Zhao, Y.; Li, Y.; Mao, J.; Yi, Z.; Mubarak, N.; Zheng, Y.; Kim, J.-K.; Chen, Q. Accelerating the dissolution kinetics of iodine with a cosolvent for a high-current zinc–iodine flow battery. *Journal of Materials Chemistry A* **2022**, *10*, 14090–14097.

(45) Chen, Y.; Guo, S.; Qin, L.; Wan, Q.; Pan, Y.; Zhou, M.; Long, M.; Fang, G.; Liang, S. Low Current-Density Stable Zinc-Metal Batteries Via Aqueous/Organic Hybrid Electrolyte. *Batteries & Supercaps* **2022**, *5*, e202200001.

(46) Wang, Z.; Zhou, M.; Qin, L.; Chen, M.; Chen, Z.; Guo, S.; Wang, L.; Fang, G.; Liang, S. Simultaneous regulation of cations and anions in an electrolyte for high-capacity, high-stability aqueous zinc–vanadium batteries. *Escience* **2022**, *2*, 209–218.

(47) Li, G.; Liu, Z.; Huang, Q.; Gao, Y.; Regula, M.; Wang, D.; Chen, L.-Q.; Wang, D. Stable metal battery anodes enabled by polyethylenimine sponge hosts by way of electrokinetic effects. *Nature Energy* **2018**, *3*, 1076–1083.

(48) Pu, J.; Shen, Z.; Zhong, C.; Zhou, Q.; Liu, J.; Zhu, J.; Zhang, H. Electrodeposition Technologies for Li-Based Batteries: New Frontiers of Energy Storage. *Advanced Materials* **2020**, *32*, 1903808.

(49) Wang, S.; Wang, Z.; Yin, Y.; Li, T.; Chang, N.; Fan, F.; Zhang, H.; Li, X. A highly reversible zinc deposition for flow batteries regulated by critical concentration induced nucleation. *Energy & Environmental Science* **2021**, *14*, 4077–4084.

(50) Feng, G.; Guo, J.; Tian, H.; Li, Z.; Shi, Y.; Li, X.; Yang, X.; Mayerich, D.; Yang, Y.; Shan, X. Probe the Localized Electrochemical Environment Effects and Electrode Reaction Dynamics for Metal Batteries using In Situ 3D Microscopy. *Advanced Energy Materials* **2022**, *12*, 2103484.

(51) Zhang, Z.; Said, S.; Smith, K.; Zhang, Y. S.; He, G.; Jervis, R.; Shearing, P. R.; Miller, T. S.; Brett, D. J. Dendrite suppression by anode polishing in zinc-ion batteries. *Journal of Materials Chemistry A* **2021**, *9*, 15355–15362.

(52) Xie, X.; Liang, S.; Gao, J.; Guo, S.; Guo, J.; Wang, C.; Xu, G.; Wu, X.; Chen, G.; Zhou, J. Manipulating the ion-transfer kinetics and interface stability for high-performance zinc metal anodes. *Energy & Environmental Science* **2020**, *13*, 503–510.

(53) Zhang, X.; Li, J.; Ao, H.; Liu, D.; Shi, L.; Wang, C.; Zhu, Y.; Qian, Y. Appropriately hydrophilic/hydrophobic cathode enables high-performance aqueous zinc-ion batteries. *Energy Storage Materials* **2020**, *30*, 337–345.

(54) Tang, B.; Shan, L.; Liang, S.; Zhou, J. Issues and opportunities facing aqueous zinc-ion batteries. *Energy & Environmental Science* **2019**, *12*, 3288–3304.

(55) Wan, F.; Zhang, L.; Wang, X.; Bi, S.; Niu, Z.; Chen, J. An aqueous rechargeable zinc-organic battery with hybrid mechanism. *Advanced Functional Materials* **2018**, *28*, 1804975.

(56) Bard, A. J.; Faulkner, L. R.; White, H. S. *Electrochemical methods: fundamentals and applications*; John Wiley & Sons, 2022.

(57) Fuller, T. F.; Harb, J. N. *Electrochemical engineering*; John Wiley & Sons, 2018; pp 120–123.

(58) Lin, D.; Rao, D.; Chiovoloni, S.; Wang, S.; Lu, J. Q.; Li, Y. Prototypical Study of Double-Layered Cathodes for Aqueous Rechargeable Static Zn–I2 Batteries. *Nano Letters* **2021**, *21*, 4129–4135.

(59) Andre, D.; Meiler, M.; Steiner, K.; Wimmer, C.; Soczka-Guth, T.; Sauer, D. Characterization of high-power lithium-ion batteries by electrochemical impedance spectroscopy. I. Experimental investigation. *Journal of Power Sources* **2011**, *196*, 5334–5341.

(60) Han, J.-H.; Khoo, E.; Bai, P.; Bazant, M. Z. Over-limiting current and control of dendritic growth by surface conduction in nanopores. *Scientific reports* **2014**, *4*, 1–8.

(61) Molinari, B. An electrochemical impedance spectroscopy study of ZnI2 redox flow batteries. M.Sc. thesis, Universitat Politècnica de Catalunya, 2019.

(62) Peng, Y.; Lai, C.; Zhang, M.; Liu, X.; Yin, Y.; Li, Y.; Wu, Z. Zn–Sn alloy anode

with repressible dendrite grown and meliorative corrosion resistance for Zn-air battery. *Journal of Power Sources* **2022**, *526*, 231173.

(63) Shi, X.; Xu, G.; Liang, S.; Li, C.; Guo, S.; Xie, X.; Ma, X.; Zhou, J. Homogeneous deposition of zinc on three-dimensional porous copper foam as a superior zinc metal anode. *ACS Sustainable Chemistry & Engineering* **2019**, *7*, 17737–17746.

(64) Guo, L.; Searson, P. C. On the influence of the nucleation overpotential on island growth in electrodeposition. *Electrochimica Acta* **2010**, *55*, 4086–4091.

(65) Sun, K. E.; Hoang, T. K.; Doan, T. N. L.; Yu, Y.; Zhu, X.; Tian, Y.; Chen, P. Suppression of dendrite formation and corrosion on zinc anode of secondary aqueous batteries. *ACS applied materials & interfaces* **2017**, *9*, 9681–9687.

(66) Sun, K. E.; Hoang, T. K.; Doan, T. N. L.; Yu, Y.; Chen, P. Highly sustainable zinc anodes for a rechargeable hybrid aqueous battery. *Chemistry–A European Journal* **2018**, *24*, 1667–1673.

(67) Mackinnon, D.; Brannen, J.; Fenn, P. Characterization of impurity effects in zinc electrowinning from industrial acid sulphate electrolyte. *Journal of applied electrochemistry* **1987**, *17*, 1129–1143.

(68) Nayana, K.; Venkatesha, T. Bright zinc electrodeposition and study of influence of synergistic interaction of additives on coating properties. *Journal of Industrial and Engineering Chemistry* **2015**, *26*, 107–115.

(69) Otani, T.; Fukunaka, Y.; Homma, T. Effect of lead and tin additives on surface morphology evolution of electrodeposited zinc. *Electrochimica Acta* **2017**, *242*, 364–372.

(70) Suresh, S.; Kesavan, T.; Munaiah, Y.; Arulraj, I.; Dheenadayalan, S.; Ragupathy, P. Zinc–bromine hybrid flow battery: effect of zinc utilization and performance characteristics. *RSC Advances* **2014**, *4*, 37947–37953.

(71) Zhang, Z.; Said, S.; Smith, K.; Jervis, R.; Howard, C. A.; Shearing, P. R.; Brett, D. J.; Miller, T. S. Characterizing batteries by in situ electrochemical atomic force microscopy: A critical review. *Advanced Energy Materials* **2021**, *11*, 2101518.

(72) Magonov, S.; Elings, V.; Whangbo, M.-H. Phase imaging and stiffness in tapping-mode atomic force microscopy. *Surface science* **1997**, *375*, L385–L391.

(73) Stark, M.; Möller, C.; Müller, D. J.; Guckenberger, R. From images to interactions: high-resolution phase imaging in tapping-mode atomic force microscopy. *Biophysical Journal* **2001**, *80*, 3009–3018.

(74) Xu, C.; Yao, Q.; Du, H.; Hong, C.; Xue, T.; Kang, Y.; Li, Q. Abnormal raman characteristics of graphene originating from contact interface inhomogeneity. *ACS Applied Materials & Interfaces* **2021**, *13*, 22040–22046.

(75) Nalam, P. C.; Gosvami, N. N.; Caporizzo, M. A.; Composto, R. J.; Carpick, R. W. Nano-rheology of hydrogels using direct drive force modulation atomic force microscopy. *Soft Matter* **2015**, *11*, 8165–8178.

(76) Xu, C.; Zhang, S.; Du, H.; Xue, T.; Kang, Y.; Zhang, Y.; Zhao, P.; Li, Q. Revisiting frictional characteristics of graphene: Effect of in-plane straining. *ACS Applied Materials & Interfaces* **2022**, *14*, 41571–41576.

(77) Xu, C.; Ye, Z.; Egberts, P. Friction hysteretic behavior of supported atomically thin nanofilms. *npj 2D Materials and Applications* **2023**, *7*, 1.

(78) Ma, M. C.; Li, G.; Chen, X.; Archer, L. A.; Wan, J. Suppression of dendrite growth by cross-flow in microfluidics. *Science advances* **2021**, *7*, eabf6941.